Spatially displaced excitation contributes to the encoding of interrupted motion by the retinal direction-selective circuit

Jennifer Ding[1,2], Albert Chen[3], Janet Chung[2], Hector Acaron Ledesma[4], David M. Berson[5], Stephanie Palmer[1,3,6]*, Wei Wei[1,2,6]*

1. Committee on Neurobiology Graduate Program, The University of Chicago
2. Department of Neurobiology, The University of Chicago
3. Department of Organismal Biology, The University of Chicago
4. Graduate Program in Biophysical Sciences, The University of Chicago
5. Department of Neuroscience, Brown University
6. Grossman Institute for Neuroscience, Quantitative Biology and Human Behavior, The University of Chicago

*Co-corresponding authors: weiw@uchicago.edu; sepalmer@uchicago.edu

Abstract

Spatially distributed excitation and inhibition collectively shape a visual neuron's receptive field (RF) properties. In the direction-selective circuit of the mammalian retina, the effects of strong null-direction inhibition of On-Off direction-selective ganglion cells (ON-OFF DSGCs) on their direction selectivity are well-studied. However, how excitatory inputs influence the On-Off DSGC's visual response is underexplored. Here, we report that the glutamatergic excitation of On-Off DSGCs shows a spatial displacement to the side where preferred-direction motion stimuli approach the soma (the 'preferred side'). Underlying this displacement is a non-uniform distribution of excitatory conductance across the dendritic span of the DSGC on the preferred-null motion axis. The skewed excitatory RF contributes to robust null-direction spiking during RF activation limited to the preferred side, a potential ethologically relevant signal to encode interrupted or discontinuous motion trajectories abundant in natural scenes. Theoretical analysis indicates that such differential firing patterns of On-Off DSGCs to continuous and interrupted motion stimuli may help leverage synchronous firing to signal the spatial location of a novel moving object in complex, naturalistic visual environments. Our study highlights that visual circuitry, even the well-defined direction-selective circuit, exploits different sets of neural mechanisms under different stimulus conditions to generate context-dependent neural representations of visual features.

Introduction

How do sensory systems convert sensory inputs into behaviorally relevant neural signals? This question has been extensively investigated in the early visual system,

where a neuron's responses to a set of parameterizable visual stimuli can be systematically probed to reveal a cell's receptive field (RF) properties in space and time. It has been increasingly appreciated that context-dependent neural mechanisms dynamically shape neuronal RFs even at the earliest stage of visual processing in the retina. The transformation from the visual input to a retinal ganglion cell's spiking output is influenced by spatiotemporal patterns of stimuli in both the RF center and surround regions, highlighting the necessity of using diverse, ethologically relevant visual stimuli for delineating RF properties and for ultimately understanding neural coding of the animal's natural environment (Chiao and Masland, 2003; Demb et al., 1999; Deny et al., 2017; Huang et al., 2019; Ölveczky et al., 2003; Takeshita and Gollisch, 2014; Turner et al., 2018).

Direction-selective ganglion cells (DSGCs) in the mammalian retina are well-studied for their motion direction selectivity. A DSGC fires maximally to visual stimuli moving across its RF in its preferred direction and is inhibited from firing by stimuli moving in the opposite, null direction (Barlow and Hill, 1963; Barlow and Levick, 1965). The direction-selective spiking of the DSGC is largely attributed to the strong null-direction inhibition that the DSGC receives from the starburst amacrine cell (SAC) (Briggman et al., 2011; Euler et al., 2002; Fried et al., 2002; Lee and Zhou, 2010; Taylor and Vaney, 2002; Wei et al., 2011; Yonehara et al., 2011). The most studied DSGC type, the On-Off DSGC, prefers motion in one of the four cardinal directions (Oyster and Barlow, 1967; Sabbah et al., 2017). They have bistratified dendritic arbors in the On and Off sublamina of the inner plexiform layer (IPL) to extract motion directions of bright and dark signals, respectively (**Figure 1A**) (Famiglietti 1983; He and Masland, 1998; Kittila and Massey, 1997).

The RF of On-Off DSGCs has been studied with conventional visual stimuli such as stationary and moving spots, bars, and gratings. For motion stimuli that traverse across the entire RF, On-Off DSGC responses remain direction-selective over a broad range of contrast, luminance, speed, and background noise levels (Barlow and Levick, 1965; Chen et al., 2016; Grzywacz and Amthor, 2007; Lipin et al., 2015; Sethuramanujam et al., 2016; Sivyer et al., 2010). However, motion stimuli restricted to the distal RF subregion on the preferred side (defined as the side from which the preferred-direction moving stimulus approaches the RF) can elicit non-directional firing (He et al., 1999; He and Masland, 1998; Rivlin-Etzion et al., 2011; Trenholm et al., 2011). Based on the responses to moving stimuli presented to different subregions of the DSGC RF, the cell's RF structure can be viewed as consisting of multiple 'DS subunits' and a 'non-DS zone' at the edge of the preferred side. However, the neural mechanisms underlying the modular and heterogenous RF subunits of On-Off DSGCs have not been elucidated. Furthermore, the functional significance of this fine RF structure is not clear.

In this study, we investigated the spatial RF structure of the mouse On-Off DSGC subtype that prefers motion in the posterior direction of the visual field (pDSGC). We found that the pDSGC spiking RF is skewed towards the preferred side of the cell for both stationary and moving stimuli, even in the absence of SAC-mediated inhibition. Combining anatomical and functional analyses, we found a spatially non-uniform glutamatergic excitatory conductance that contributes to this spatial displacement. As a result of the displaced RF, moving stimuli that only activate the preferred side of the pDSGC RF trigger robust firing during either preferred or null direction motion. Theoretical analyses of the On-Off DSGC population response allow us to speculate about the ethological relevance of the displaced RF in processing complex natural scenes, suggesting that it can allow for better estimation of object location when a moving object emerges from behind an occluder. We term this type of motion 'interrupted motion' to distinguish it from more standard constant motion stimuli. This phenomenon might also allow synchronous firing from different sub-types of DSGCs to serve as a useful alarm signal in complex scenes.

Results

Glutamatergic excitation of the On-Off pDSGC is spatially asymmetric relative to the soma

To investigate the spatial distribution of excitatory inputs to On-Off pDSGCs, we targeted pDSGCs in the Drd4-GFP transgenic mouse line to record their On spiking and synaptic responses to the light onset of flashing stationary bright spots presented to the periphery of the DSGC RF. These spots were 110 μm in diameter and centered 165 μm from the soma of the recorded DSGC (**Figure 1B**, schematic). Measurement of the average radius of pDSGC On dendrites (88.1, SEM 13.9 μm, from 25 cells, see Methods) indicates that the spot mostly covered areas beyond the dendritic span of these cells. For each cell tested, we also presented a moving bar stimulus to confirm its directional tuning to posterior-direction motion in the visual field.

The spot stimulus delivered to the pDSGC RF periphery uncovered an asymmetric RF organization: the maximal spiking was triggered by the spot shown on the preferred side of the cell, and the minimal response was triggered to the spot shown on the null side (**Figure 1B**), indicating a spatial displacement of this aspect of the RF relative to the soma. To quantify the extent of this RF displacement, we calculated a region selectivity index (RSI) defined as the normalized difference of the maximum response (Max) and the response to the spot presented in the opposite region (Opp) (see Methods). pDSGCs exhibit a robust spatial bias of their spiking RFs to the preferred side (**Figures 1C** "Control" and **S1A**).

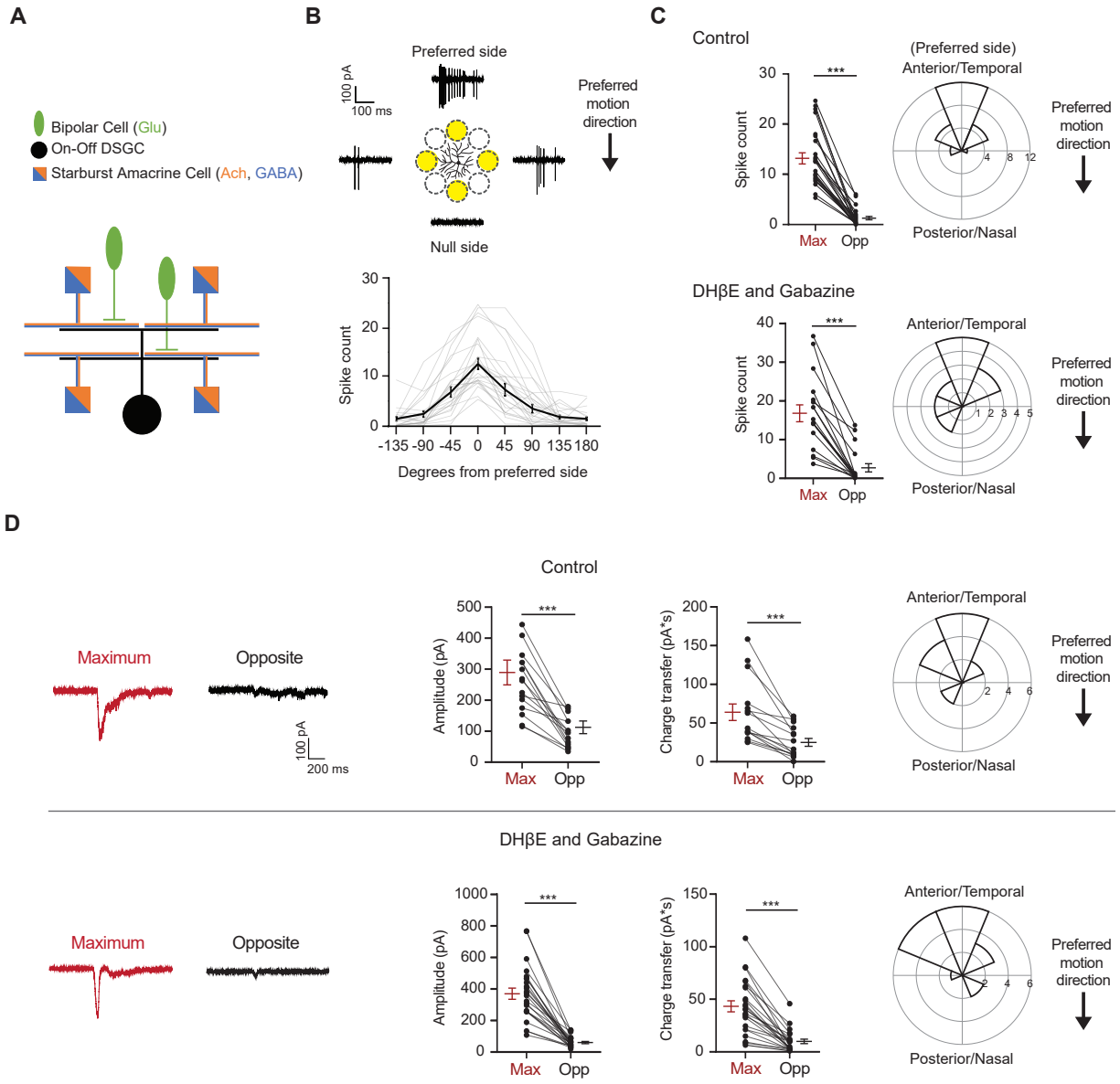

Figure 1. Drd4-GFP labeled pDSGCs have spatially asymmetric glutamatergic receptive fields.

(A) Schematic showing types of presynaptic neurons to an On-Off DSGC and the neurotransmitters they use. **(B)** Top: Example On spiking responses of a pDSGC to four different peripheral spots presented around dendritic span. Bottom: Individual (gray) and mean (black) pDSGC On spike counts evoked by spots presented at different locations (25 cells). **(C)** Top left: Pairwise comparison of mean spike counts in regions evoking the maximum number of spikes (Max) and the opposite region (Opp) in the control condition (25 cells). Top right: Polar histogram of Max region locations aligned to the preferred-null motion axis. Radius indicates number of cells. Bottom: Same as in top but experiments performed in DHβE + Gabazine (18 cells). **(D)** Left: Example On EPSC responses to spots shown in the regions evoking the strongest EPSCs (Max) and the opposite region (Opp) in control (top) and in DHβE + Gabazine (bottom). Middle: Pairwise comparisons of EPSC amplitude and charge transfer to spots presented in the Max region and Opp region (Control: 15 cells; DHβE + Gabazine: 24 cells). Right: Polar histograms of Max region locations determined by EPSC charge transfer aligned to the preferred-null motion axis. Radius indicates number of cells. Summary statistics are mean ± SEM, ***$p < 0.001$.

141 Because a well-documented asymmetry in the direction-selective circuit is the
142 asymmetric inhibition from SACs to DSGCs, we next tested whether the displacement
143 of the pDSGC spiking RF is eliminated by blocking SAC inputs. We perfused the retina
144 with the nicotinic antagonist DHβE and the $GABA_A$ receptor antagonist gabazine to
145 block these inputs. Under this condition, we still observed a spatial asymmetry in
146 pDSGC spiking activity evoked by the flashing spots (**Figures 1C, S1A and S1B**,
147 "DHβE and Gabazine"), indicating a spatial displacement of glutamatergic excitation of
148 the pDSGC in the absence of SAC influence.
149
150 To directly measure the strength of excitatory inputs to pDSGCs at different
151 stimulus locations, we performed whole-cell voltage clamp recordings of excitatory
152 postsynaptic currents (EPSCs) evoked by peripheral flashing spots. Consistent with the
153 pattern of pDSGC spiking activity, spot-evoked EPSCs show a spatial bias towards the
154 preferred side (**Figures 1D and S1C**, "Control"). Isolation of the glutamatergic
155 component of the EPSC by the addition of DHβE and gabazine confirms the persistence
156 of the spatial asymmetry, indicating that the glutamatergic excitation of the pDSGC is
157 not isotropic but is spatially displaced relative to the soma (**Figures 1D, S1B and S1C**,
158 "DHβE and Gabazine"). This pharmacological manipulation also rules out potential
159 confounding influences of asymmetric inhibitory inputs from SACs on pDSGC EPSCs
160 during voltage clamp recordings due to space clamp.
161
162 We investigated the Off responses in tandem with the On responses and found
163 the same RF displacement in all conditions (**Figures S1D – S1F**). We focused on the
164 On response for the remaining experiments.
165
166 **Non-uniform excitatory conductance across the preferred-null motion axis**
167 **contributes to the asymmetric glutamatergic RF**
168
169 An asymmetric excitatory RF of a retinal neuron may result from asymmetric
170 dendritic arbors and/or an asymmetric distribution of excitatory synaptic inputs across its
171 dendritic field. To examine the relationship between pDSGC dendritic morphology and
172 glutamatergic inputs, we performed two-photon imaging of dye-filled dendritic arbors
173 after recording glutamatergic EPSCs evoked by the peripheral flashing spot stimulus
174 described above (**Figures 2A and 2B**). Consistent with previous studies, On dendritic
175 arbors of pDSGCs do not exhibit a salient or consistent bias relative to the cell's
176 preferred motion direction. The total dendritic length or the number of dendritic
177 branching points does not significantly differ between the preferred and null sides of the
178 pDSGC dendritic field (**Figures 2C, 2D and S2A**). This apparent randomness of
179 dendritic arbor distribution relative to the cell's preferred motion direction contrasts with
180 the previously reported mouse On-Off DSGC subtype preferring motion in the superior

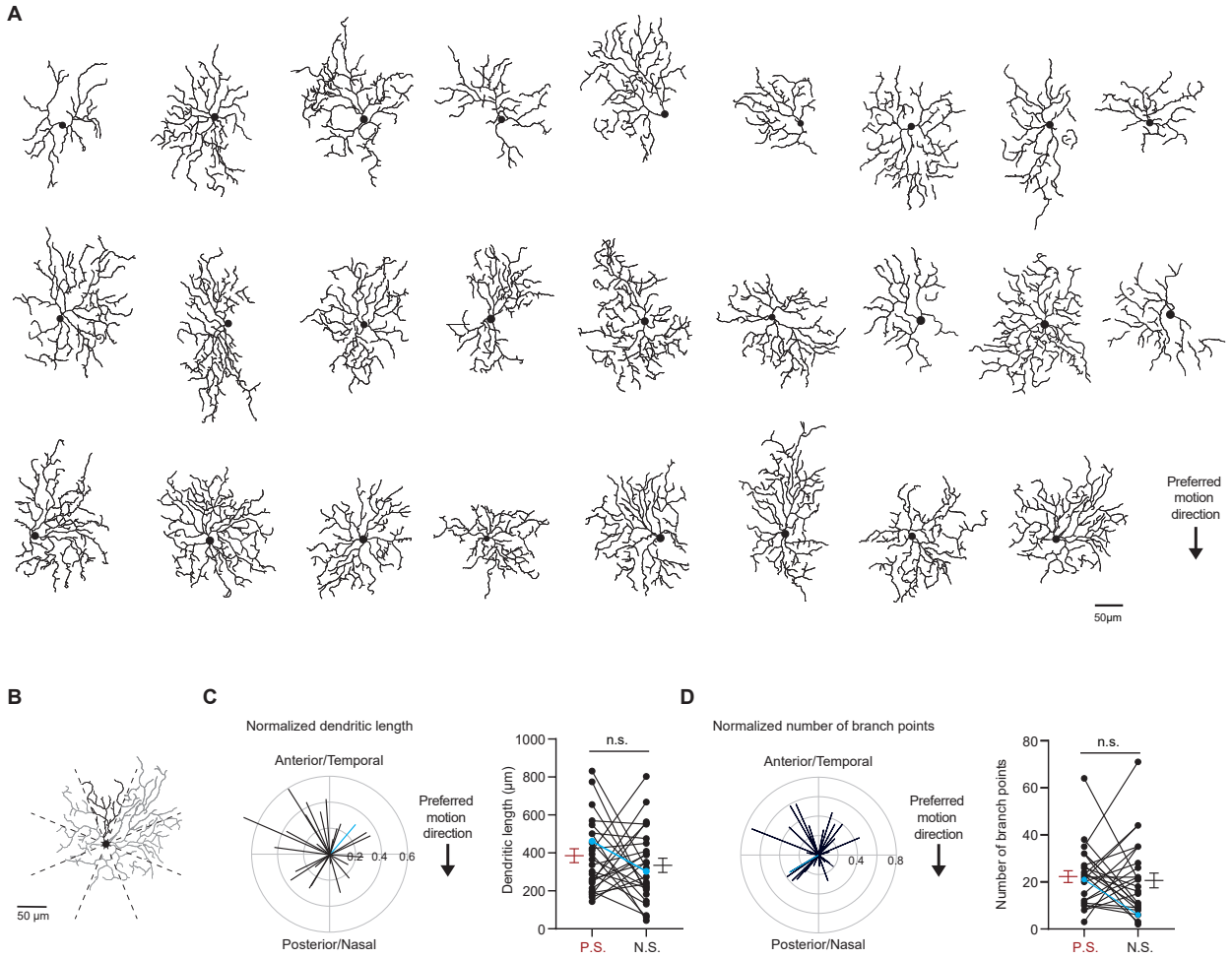

Figure 2. pDSGC dendritic morphology does not show a spatial bias towards the preferred side

(A) Traced On layer dendritic morphologies of pDSGCs aligned to their preferred-direction motion. **(B)** Example morphology of a pDSGC cell divided into eight sectors for calculating normalized dendritic length vector. **(C)** Left: Normalized vector sum of dendritic length aligned to pDSGCs' preferred direction motion. Right: Pairwise comparison of dendritic length on the preferred vs null sides of each cell (26 cells, p = 0.51). Blue represents example cell in **B**. **(D)** Left: Normalized vector sum of branch points aligned to pDSGCs' preferred direction motion. Right: Pairwise comparison of branch points on the preferred vs null side (26 cells, p = 0.68). Blue represents example cell in **B**.

direction that have dendritic arbors strongly displaced to the null side of the soma (Kay et al., 2011; Trenholm et al., 2011).

Although pDSGC dendritic fields are not strongly skewed towards the preferred side of the soma, a quantitative comparison between pDSGC dendritic arbor distribution and the distribution of their glutamatergic EPSCs has not been performed. We found a non-random skew of the pDSGC dendritic length and number of branch points towards the regions corresponding to spots evoking the strongest glutamatergic EPSCs (**Figure S2B**). However, this structural bias is not correlated with the bias in EPSC strength (**Figure S2C**), suggesting that dendritic arbor density alone cannot fully explain the displacement of the pDSGC glutamatergic RF.

To further explore the relationship between the pDSGC glutamatergic RF and its dendritic distribution, we performed another set of experiments to obtain a more complete RF map. First, the preferred direction of each cell's spiking activity was determined by loose cell-attached recordings using a moving bar stimulus with no synaptic blockers. Next, peripheral flashing spots were used to estimate the spatial displacement of the pDSGC glutamatergic RF in the presence of nicotinic and GABAergic receptor antagonists (DHβE + Gabazine) as described above. Then, a smaller, 20 μm diameter bright stationary spot was repeatedly flashed at random locations within a 11-by-11 220 μm square grid centered on the pDSGC soma. A heatmap of glutamatergic EPSC charge transfer evoked by the small flashing spot was generated and overlaid with the reconstructed dendritic arbors for each pDSGC (**Figure 3A**).

RF mapping with small flashing spots also revealed a spatial displacement of glutamatergic EPSC distribution that aligns well with the displacement determined by larger spots presented to the pDSGC periphery (**Figure 3B**). Similar to the displacement pattern revealed by stimulation of the RF periphery, the strongest glutamatergic EPSCs are preferentially located on the preferred side of pDSGC somas (**Figure 3C**). Notably, for most cells, the center of the glutamatergic EPSC RF is displaced from the center of the dendritic field (**Figure S3A – S3B**), indicating additional mechanisms underlying the glutamatergic RF displacement apart from the dendritic arbor distribution.

We further examined the strength of the glutamatergic input across the pDSGC On dendritic field (**Figure 3D**). We normalized the EPSC charge transfer by the total dendritic length in a circle with a 60 μm diameter centered on each small flashing spot. This provides an estimate of the strength of glutamatergic inputs per unit dendritic length, or "EPSC density", at each stimulus location. When we calculated the density along the axis of maximal glutamatergic RF displacement, we found that the EPSC

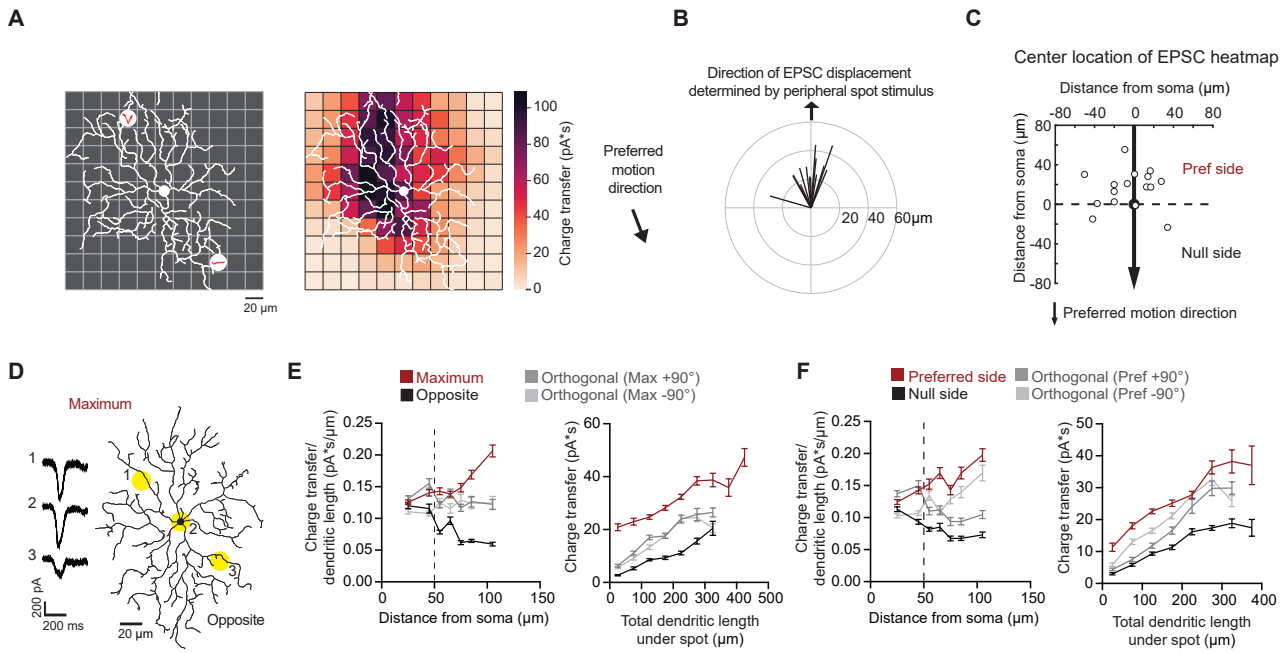

Figure 3. Non-uniform glutamatergic synaptic excitation across pDSGC dendritic span contributes to skewed excitatory receptive field.
(A) Left: Schematic for small spot RF mapping experiment in DHβE + Gabazine. Middle: Example heat map. Right: Preferred motion direction of the example cell. **(B)** Vector sum plot of EPSC charge transfer center of mass determined by small spot RF mapping aligned to the region where a peripheral spot evokes the maximum glutamatergic EPSC (upward arrow). **(C)** Spatial locations showing centers of mass of glutamatergic excitatory charge transfer obtained from experiments illustrated in **A** aligned to each cell's preferred motion direction (15 cells). **(D)** Example EPSC responses to spots presented to a pDSGC along the maximum-opposite axis of glutamatergic RF displacement. **(E)** Left: "EPSC current density" (i.e. ratio of charge transfer per dendritic length) versus distance from soma along the maximum-opposite axis of glutamatergic RF displacement (16 cells, ***$p < 0.001$) as well as the orthogonal regions. Right: Summary plot of glutamatergic charge transfer as a function of total dendritic length centered around the flashing spot for spots shown more than 50 µm away from the soma (16 cells, ***$p < 0.001$). **(F)** Same as **E** but along the preferred-null motion axis (15 cells, charge transfer/dendritic length vs distance from soma **$p = 0.0026$, charge transfer vs dendritic length ***$p < 0.001$).

density on the displaced side of the dendritic field is larger than the corresponding region on the opposite side (**Figure 3E**, left). From 50 μm away from the soma, spots on the side corresponding to the maximum displacement (Maximum) yield stronger EPSCs than spots on the opposite side (Opposite), while controlling for the same dendritic length (**Figure 3E,** right). This heterogeneity in EPSC density across the dendritic span persists when comparing EPSC responses along the preferred-direction motion axis of the cell (**Figure 3F**). Analysis of the peak amplitudes showed similar results as charge transfer (**Figures S3C – S3D**).

Next, we asked what mechanisms could underlie the non-uniform excitatory conductance across the dendritic span, focusing on the influence of bipolar cell inputs onto the DSGCs. A potential explanation for stronger excitatory responses to stimuli presented on the preferred side would be a higher concentration of bipolar cell ribbon synapses on the preferred side. To quantify the distribution pattern of ribbon synapses across the DSGC dendritic field, we performed a connectomic analysis of ribbon input sites on three On-Off DSGCs tuned to the horizontal motion axis (**Figure 4A**) using a previously published serial block-face scanning electron microscopy (SBEM) dataset (Ding et al., 2016). The preferred direction of the traced DSGCs was determined by the orientation of starburst inputs onto these cells (**Figure 4B**). The posterior-anterior axis was estimated by several cell types traced in the same block whose dendritic arbors are strongly biased in the orthogonal superior-inferior axis including Jam-B RGCs (Kay et al., 2011) and F-RGCs (Rousso et al., 2016). We found no marked gradient in ribbon density across the preferred-null motion axis of the three cells (**Figures 4C – 4E, S4A – S4B),** suggesting that the gradient in EPSC density across this axis is not determined by the density of bipolar inputs.

In addition to ribbon density, we also examined the time course of glutamatergic EPSCs in the presence of DHβE and Gabazine along the axis of maximal glutamatergic RF displacement and along the preferred-null motion axis. We found no significant differences in the latency, rise and decay times in EPSC waveforms across the axis of maximal glutamatergic RF displacement in response to the small flashing spots (**Figures 4F – 4H,** left panels). In addition, we did not detect a monotonic change in glutamatergic EPSC kinetics along the preferred-null motion axis in DHβE and Gabazine (**Figures 4F – 4H,** right panels) or in DHβE only (**Figures S4C and S4D**). Similar glutamatergic EPSC waveforms across the pDSGC dendritic field contrast with a previous study of On DSGCs reporting a gradient of EPSC temporal kinetics from slow/sustained to fast/transient corresponding to different bipolar cell subtypes along the preferred-null motion axis to implement a Hassenstein-Reichardt-Detector-like mechanism for their direction selectivity (Matsumoto et al., 2019).

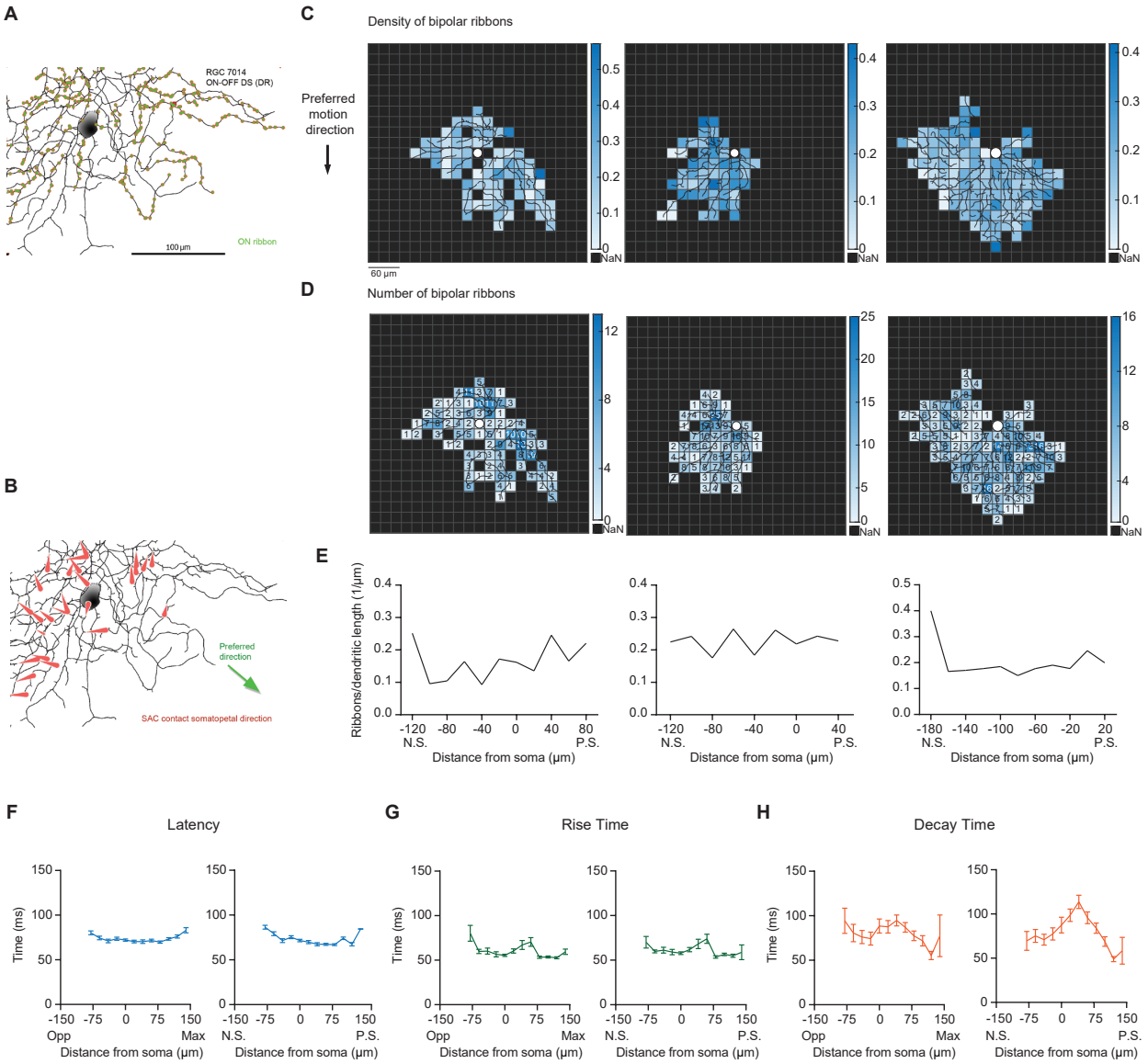

Figure 4. Bipolar cell ribbon synapse density and glutamatergic EPSC kinetics do not systematically vary along the axis of RF displacement.
(A) Ribbons from On bipolar cells on an example On-Off DSGC. **(B)** Starburst amacrine cell inputs onto example On-Off DSGC. Red arrows indicate the direction and location of the SAC inputs on the DSGC dendrites. **(C)** Density map of bipolar ribbon synapses for 3 example On-Off DSGCs with estimated preferred directions along the posterior-anterior axis (see Methods). The soma location is indicated by the white spot in the center. **(D)** Bipolar ribbon heat map for the 3 example cells, respectively. Number in each square indicates the number of ribbons detected in that square. **(E)** Quantification of ribbon density across the preferred-null axis, respectively. The soma location is at 0. (N.S. = null side, P.S. = preferred side). **(F)** Left: Summary of latency of glutamatergic EPSC responses along the maximum-opposite axis (Max = maximum glutamatergic EPSC region, Opp = opposite region)(16 cells, $p = 0.75$). Right: Summary of latency along the preferred-null motion axis (N.S. = null side, P.S. = preferred side)(16 cells, $p = 0.88$). **(G)** Same as in **F**, except for rise time (10% - 90%). (Left: $p = 0.12$, right: $p = 0.21$, 16 cells). **(H)** Same as in **F**, except for decay time (90% - 30%). (Left: $p = 0.25$, right: $p = 0.26$, 16 cells).

314 **Null-direction response emerges during partial activation of the displaced pDSGC**
315 **RF**
316
317 Because On-Off DSGCs are thought to be dedicated to encoding object motion,
318 we next asked how the displaced excitatory RF of the pDSGC revealed by the
319 stationary flashing stimuli contributes to motion processing. We reasoned that because
320 conventional simple motion stimuli such as moving bars and drifting gratings traverse
321 the entire RF of the pDSGC, SAC-mediated inhibition would exert a dominant influence
322 on pDSGC spiking by strongly suppressing the pDSGC null-direction response.
323 However, when motion trajectories are more complex, as often occurs in the natural
324 environment, the displaced excitatory pDSGC RF may confer additional characteristics
325 to the cell's motion encoding. Therefore, we investigated how the direction-selective
326 circuit would process interrupted motion because moving objects in the natural
327 environment often pass behind occluders or start moving after being stationary.
328
329 To examine if the displaced excitatory RF of the pDSGC plays a role in encoding
330 interrupted motion, we created an occluded motion stimulus where a moving bar
331 disappeared behind a central occluder 220 μm in diameter (**Figure 5A**). The occluder
332 covered the dendritic span of the pDSGC and a substantial portion of its RF center. In
333 contrast to the full-field motion stimuli, the occluded motion stimulus caused both
334 preferred and null-direction On spiking responses (**Figures 5B and S5A**). These
335 responses are only evoked when the bar travels in the preferred side, which
336 corresponds to the displaced side of the pDSGC RF (**Figure 5B**, middle row). In
337 contrast, no spiking response is evoked when the bar moves across to the null side
338 beyond the occluder (**Figures 5B,** bottom row, **5C**). To test whether this regional
339 difference is due to the asymmetric wiring between SACs and DSGCs, we blocked the
340 cholinergic and GABAergic transmission with DHβE and gabazine and saw that the
341 regional difference persisted (**Figures 5C and S5B**). Consistent with the spiking
342 pattern, the EPSC responses also reflected this regional asymmetry (**Figure 5D**).
343
344 Moreover, we blocked $GABA_C$ receptor activity, glycine receptor activity, and
345 gap-junction coupling with TPMPA, strychnine and MFA, respectively, and found that
346 the spatial asymmetry of the spike response remains during the occluded motion
347 stimulus (**Figures S5C – S5E**). Based on these pharmacology results, we conclude that
348 the asymmetric glutamatergic RF of the pDSGC contributes to robust spiking in both
349 null and preferred directions when the preferred side of the RF is activated by the
350 occluded motion stimulus.
351

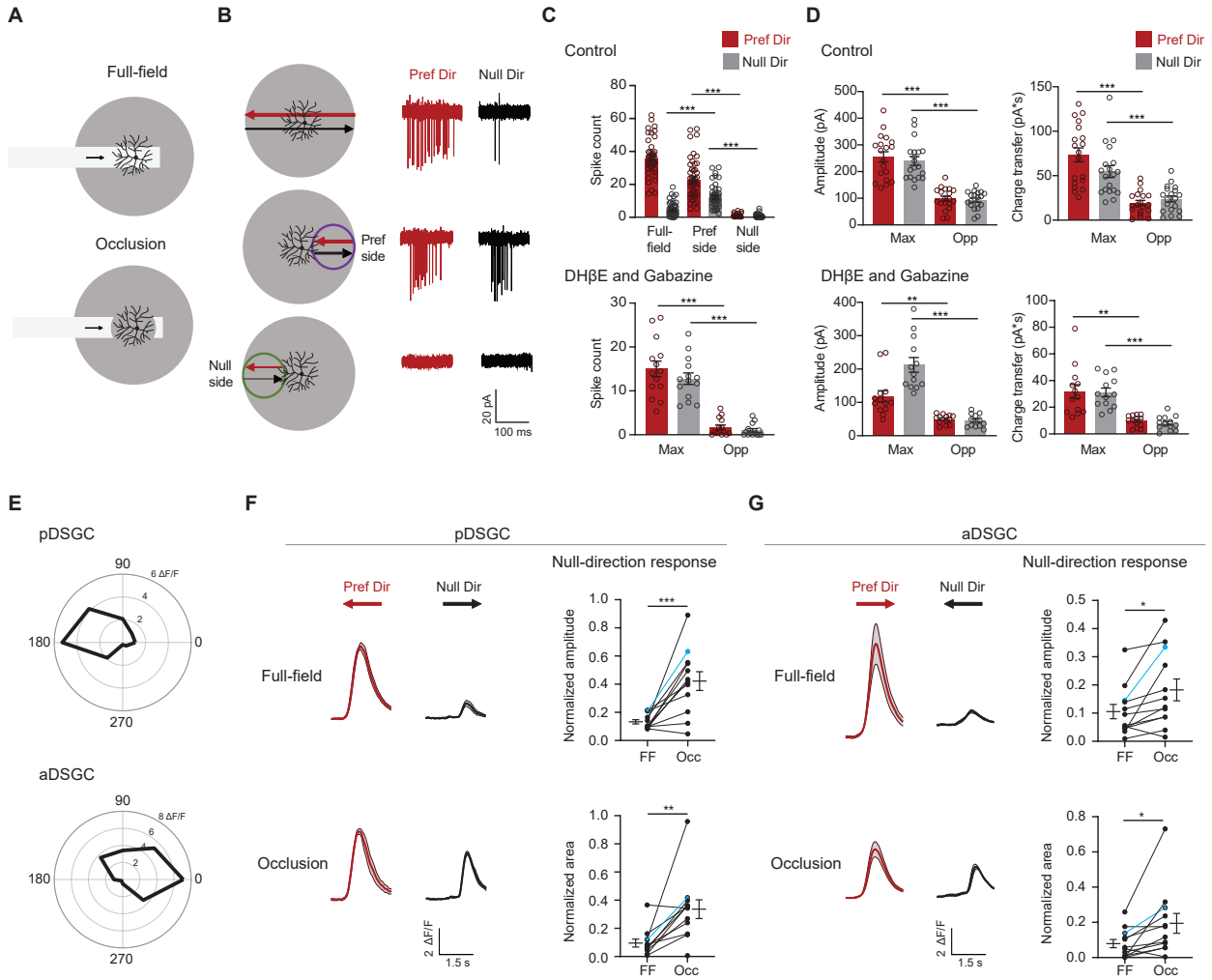

Figure 5. Displaced excitatory receptive field contributes to null-direction responses in the preferred region. (A) Full-field moving bar and occluded bar stimuli. **(B)** Example On spiking responses of a pDSGC to full-field bar (top) and occluded bar stimulus (middle, bottom) moving in the preferred (red) and null (black) directions. **(C)** Top: Mean spike counts of pDSGCs to the full-field moving bar (full-field) and the occluded moving bar on the preferred side and null side (48 cells). Bottom: Mean spike counts in DHβE + Gabazine to the occluded bar stimulus in the region evoking the maximum spiking (Max) and the opposite region (Opp) (13 cells). **(D)** Mean pDSGC EPSC peak amplitude and charge transfer in the region evoking the maximum response (Max) and the opposite region (Opp) in the control (top, 19 cells) and DHβE + Gabazine (bottom, 13 cells) conditions. (In DHβE + Gabazine: Pref Dir – Max vs Pref Dir – Opp amplitude **p = 0.0028, Pref Dir – Max vs Pref Dir – Opp charge transfer **p = 0.0012). **(E)** Top: Example directional tuning curve of GCaMP6 signal of a pDSGC. Bottom: Example tuning curve of an aDSGC. **(F)** Top left: Example GCaMP6 fluorescence traces of a pDSGC for the full-field moving bar in the preferred (red) and null (black) directions. Bottom left: Example GCaMP6 traces of the cell for the occluded bar stimulus. Top right: Normalized amplitude of the posterior-preferring cell null-direction response during the full-field bar and the occluded bar (12 cells). Bottom right: Normalized area of the null-direction response during the full-field bar and the occluded bar (12 cells, **p = 0.0035). **(G)** same as in **F**, for aDSGCs. (12 cells, normalized amplitude *p = 0.013, normalized area *p = 0.019). Summary statistics are mean ± SEM, ***p < 0.001 except where specified otherwise.

374 Since there are two On-Off DSGC subtypes that are tuned to the opposite
375 directions along the posterior-anterior axis, we investigated if the anterior-direction-
376 selective DSGC (aDSGC) exhibits the same null-direction response pattern to the
377 occluded motion stimulus as the pDSGC. To identify both DSGC subtypes, we
378 performed calcium imaging of GCaMP6-expressing RGCs in another transgenic mouse
379 line carrying Vglut2-IRES-Cre and floxed GCaMP6f (**Figure S6A**) during the full-field
380 moving bar stimulus. We then used an online analysis to identify aDSGCs and pDSGCs
381 based on the directional tuning of their calcium signals to the anterior and posterior
382 motion directions (**Figures 5E and S6B – C**). Next, we centered the occluded motion
383 stimulus on individual aDSGC and pDSGC somas and performed calcium imaging
384 during the occluded motion stimulus. Consistent with pDSGC spiking activity, a
385 significant null-direction calcium response of the pDSGCs was evoked when the
386 occluded moving bar traveled across the receptive field to the preferred side of the RF
387 (**Figures 5F and S6D**). Notably, aDSGCs also exhibited a null-direction response to the
388 occluded motion stimulus that is similar to that of pDSGCs (**Figure 5G and S6D**),
389 indicating that aDSGC RFs are also displaced to the preferred side.
390
391 The above results show that continuous motion interrupted by a stationary
392 occluder in the center of the pDSGC's RF causes unexpected null-direction spiking as
393 the bar emerges from behind the occluder into the preferred side of the pDSGC RF.
394 However, this occluded motion stimulus cannot distinguish whether the interruption itself
395 or only the start position of the emerging bar was necessary for the null-direction
396 response. Therefore, we created a stimulus where a growing edge of a moving bar
397 would emerge at different locations along the preferred-null motion axis of the cell
398 (**Figure 6A**). For the null-direction moving bar, there is an increase in both the spike
399 number and the firing rate as the starting position of the moving bar is located past the
400 soma on the preferred side of the pDSGC RF (**Figures 6A – 6C**). Thus, the emergent
401 growing edge caused null-direction spiking of pDSGCs in a similar pattern as the
402 moving bar emerging behind the central occluder. These results illustrate that the null-
403 direction response of the pDSGC during the occluded motion stimulus is dependent on
404 the position in the receptive field from which the moving edge emerges, not the previous
405 motion approaching the occluder.
406
407 **Null-direction responses of DSGCs during partial activation of their RFs can be**
408 **useful for decoding object location**
409
410 Because of their displaced RFs, pDSGCs generate robust spiking activity in both
411 the preferred and null directions when a moving object appears and starts moving on
412 the preferred side of the cell's RF, as when an object emerges from behind an occluder
413 positioned over the cell's soma. We asked whether this prima facie aberrant signaling
414

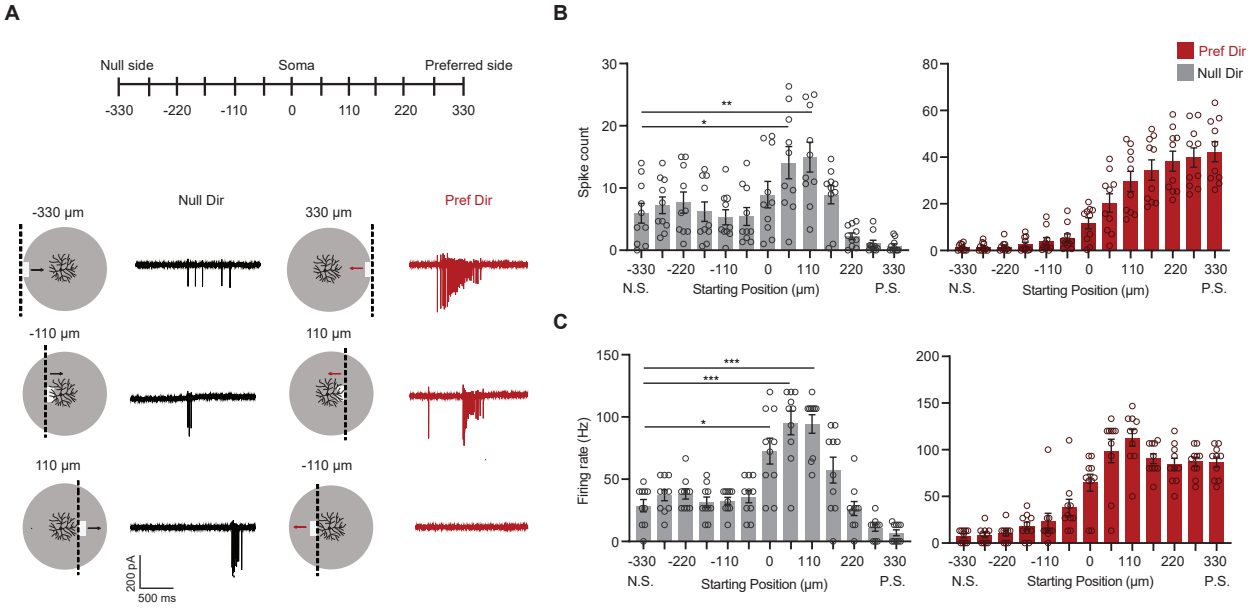

Figure 6. Null-direction response is dependent on start position of emerging bar
(A) Schematic of moving bars emerging from different locations along the DSGC's preferred-null motion axis and example spiking responses. The soma location is at 0. Vertical dashed lines on the schematic indicate the positions of the emerging leading edge of the moving bar. **(B)** Mean spike counts (top, null direction: -330 vs 55 *p = 0.012, -330 vs 110 **p = 0.0088) and **(C)** firing rates (bottom, null direction: -330 vs 0 *p = 0.014) to bars emerging from different locations along the preferred-null axis (10 cells). Summary statistics are mean ± SEM, ***p < 0.001 except where specified otherwise.

426 can have a functional role relevant to the behavioral goals of the organism. We
427 hypothesize that partial RF activation of a DSGC at a given region in visual space may
428 provide precise information about the spatial position of a moving object along an
429 interrupted motion trajectory. In particular, if a moving object emerging from behind an
430 occluder activates the preferred side of an On-Off DSGC's RF, this DSGC would
431 generate a null-direction spiking response together with the preferred-direction
432 response of a nearby On-Off DSGC subtype preferring the opposite motion direction
433 (**Figure 7A**). Such synchronous spiking activity between DSGCs of opposite preferred
434 directions at the location of the occluder could yield a stronger and more localized
435 spatial signal at the population level in response to interrupted motion.
436
437 To test how the null-direction response during interrupted motion might enhance
438 downstream estimation of stimulus position, we simulated the spiking responses of
439 pDSGCs in a one-dimensional model consisting of On-Off DSGC subtypes that prefer
440 opposite motion directions on the posterior-anterior axis (aDSGCs and pDSGCs, **Figure**
441 **7A**). One hundred cells of each subtype were arranged along the preferred motion axis
442 of both groups such that the spatial positions of the two subtypes were uncorrelated.
443 We simulated a bright edge moving along this axis in a single direction at a constant
444 velocity under both uninterrupted and interrupted motion conditions and analyzed the
445 On response to the edge. The mean spiking response of each DSGC was modeled as a
446 rectified sine wave with parameters obtained from our experimental data (**Figures 7B –**
447 **7D** and **S7**), and sub-Poisson trial-to-trial variability was introduced to the mean spiking
448 response on each trial (**Figure S7D**). The spatial positions of the DSGCs were shuffled
449 in each simulation block to allow us to average over different spatial arrangements of
450 the RFs.
451
452 Using a population vector decoder (see Methods), we compared the scenario in
453 which none of the DSGCs were occluded (full-field) with the scenario in which a single
454 occluder was placed over a DSGC that prefers the direction opposite to the motion
455 direction of the moving edge (occlusion). The occluded DSGC's spiking response to an
456 edge moving in its null direction certainly degrades direction estimation and appears to
457 be a defect of the direction-selective circuit. Nevertheless, the coincidence of this null-
458 direction response from a pDSGC and the preferred-direction responses of neighbor
459 aDSGCs that prefer motion in the anterior direction reduces the error in the population
460 estimate of the edge's spatial position by ~15 percent (**Figure 7E**). The synchronous
461 firing may, itself, also be a useful alarm signal to trigger attention downstream of the
462 retina, independent of the precise position information it might additionally convey. In
463 conjunction with other retinal cell types in the mouse that encode the location of moving
464 objects, On-Off DSGCs may contribute to fine spatial discrimination during interrupted
465 motion in complex natural scenes.

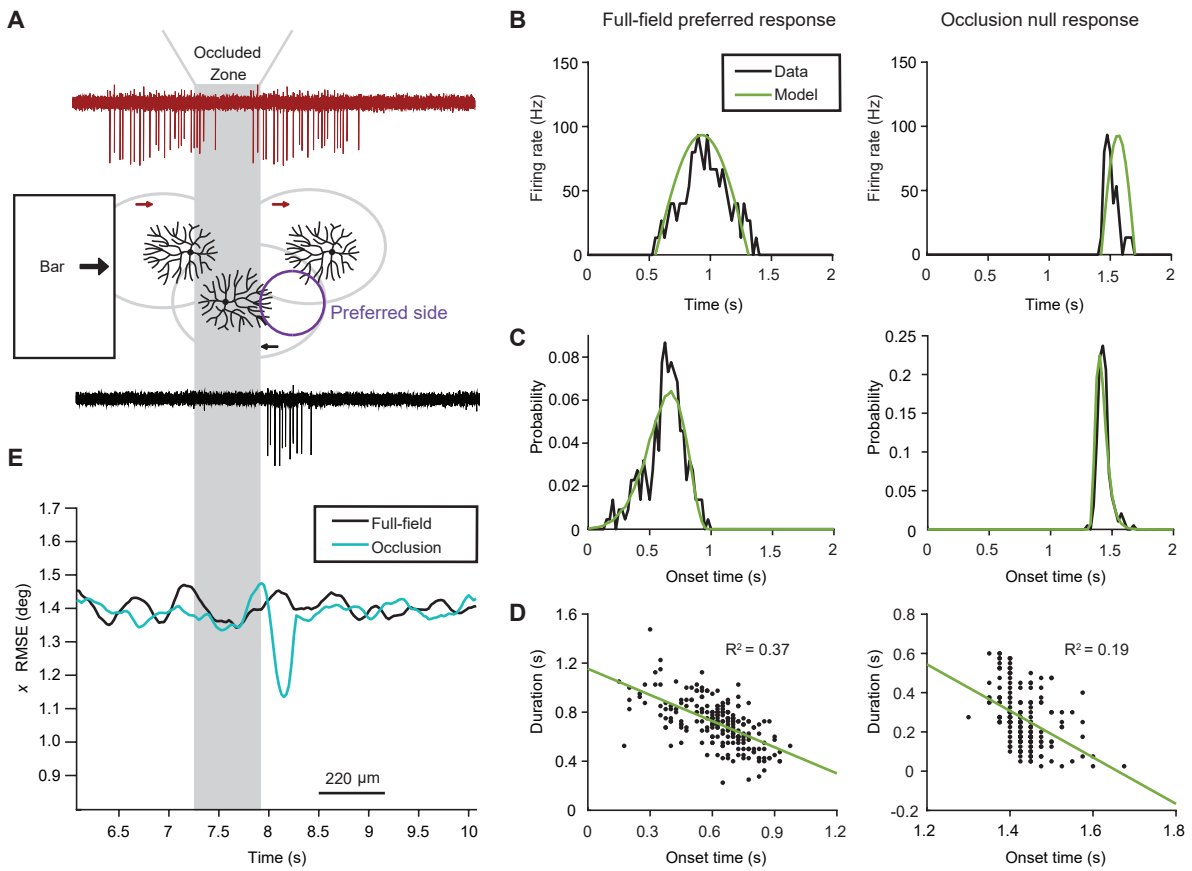

Figure 7. Null-direction spiking of On-Off DSGCs during the occluded motion stimulus improves position estimation.
(A) Schematic of one-dimensional DSGC population model along with example spike trains for two pDSGCs (red trace showing their preferred-direction responses) and an a DSGC (black trace showing its null-direction response). An occluder 220 µm wide (shaded bar) was centered on the soma of the aDSGC. **(B)** Example half sine wave fits (green) to PSTHs obtained from experimental data (left: full-field, 73 cells; right: occlusion, 69 cells). **(C)** Fits to probability distributions of spike response onset times (left: full-field, 73 cells; right: occlusion, 69 cells). **(D)** Linear correlation between spike response duration and spike response onset time (left: full-field, 73 cells; right: occlusion, 69 cells). **(E)** Root-mean-square error in estimating the position of the light bar's leading edge for full-field (black) and occluded (blue) motion.

481 **Discussion**
482
483 Our study reveals a new form of asymmetry in the direction-selective circuit: a
484 spatial displacement of glutamatergic inputs to the preferred side of the On-Off pDSGCs
485 due to a non-uniform distribution of synaptic conductances across the pDSGC dendritic
486 span. The impact of this displaced excitation on DSGC spiking is demonstrated by using
487 moving stimuli with interrupted trajectories, a feature abundant in natural scenes. In
488 contrast to full-field continuous motion which maximizes the contribution of SAC-
489 mediated null-direction inhibition, occluded motion stimuli reduce the contribution of
490 SAC-mediated inputs to allow the excitatory receptive field to dominate the spiking
491 response in a non-directional manner when only part of the RF is stimulated. Therefore,
492 an On-Off DSGC's response is dynamically shaped by visual stimulus-dependent
493 interactions of excitatory and inhibitory synaptic circuitries and may flexibly represent
494 motion direction or motion location in a context-dependent manner.
495
496 The non-isotropic excitation of the pDSGC alludes to a more sophisticated set of
497 wiring and signaling mechanisms from the bipolar cell population (Franke et al., 2017).
498 A detailed explanation of the glutamatergic RF displacement awaits future studies. The
499 gradient of glutamatergic current density across the pDSGC dendritic span may arise
500 from a number of possible scenarios including varying strengths of individual
501 glutamatergic synapses, heterogeneous membrane properties across pDSGC dendritic
502 field, and contribution from Vglut3+ amacrine cells (Kim et al., 2015; Lee et al., 2016).
503 Although our study focuses on the On component of the direction-selective circuit, we
504 observed a similar pattern of RF displacement for the pDSGC Off response, suggesting
505 similar mechanisms operating in the Off layer of the IPL.
506
507 We combined experimental recordings and theoretical analysis to obtain insights
508 into the nature of the visual information encoded by On-Off DSGCs during interrupted
509 motion. Previous theoretical analysis has addressed the encoding of motion direction by
510 DSGCs at the population level (Fiscella et al., 2015; Kühn and Gollisch, 2019;
511 Zylberberg et al., 2016). In this study, we explored a new hypothesis that On-Off DSGC
512 population activity contains information about both the direction and the location of a
513 moving object. When a moving object emerges from an occluder, the null-direction
514 response of an On-Off DSGC is synchronized with the preferred-direction responses of
515 On-Off DSGCs preferring the opposite direction with overlapping spatial RFs. Since
516 synchronized activity among RGCs has been shown in multiple species to encode
517 ethologically relevant visual information (Ishikane et al., 2005; Schwartz et al., 2007), it
518 is possible that the highly localized and synchronized firing of oppositely tuned DSGC
519 types may render the object emerging from behind the occluder more salient by
520 enhancing positional information. For instance, when a predator moves suddenly from

behind an occluding object, a mouse may prioritize information about the predator's position over its direction of movement. The encoding of both motion direction and spatial location may be particularly useful in the superior colliculus (SC) where On-Off DSGC inputs are targeted to the superficial layer (Huberman et al., 2009; Shi et al., 2017), as the colliculus supports threat evaluation and visually guided eye and head movements (Ito and Feldheim, 2018).

It is likely that other ganglion cell types, such as W3-RGCs and HD-RGCs (Kim et al., 2010; Zhang et al., 2012; Jacoby and Schwartz, 2017), also participate in fine spatial discrimination and motion encoding. However, because no other ganglion cell types are known to project to the same regions of the dorsal lateral geniculate nucleus (dLGN) and the SC as On-Off DSGCs (Huberman et al., 2009; Kay et al., 2011; Sanes and Masland, 2015; Shi et al., 2017), they may not participate in the same visual processing tasks as On-Off DSGCs or may provide complementary information about spatial location of moving objects. The synchronous firing of two typically asynchronous On-Off DSGC subtypes may, in and of itself, form a useful attention signal downstream of the retina. Elucidating the roles of diverse RGC types in motion encoding requires a thorough understanding of visual signal transforms along pathways and how the visual system instructs visually guided behavior.

Together, our study demonstrates how a visual neuron's response is determined by stimulus-dependent assembly of circuit components, and thereby provides insights into the neural basis of context-dependent visual encoding of complex natural environments.

Acknowledgements

We thank Chen Zhang for managing the mouse colony and Dr. John Maunsell, Mathew Summers, Malak El-Quessny, Siwei Wang, and Benjamin Hoshal for advice on the manuscript. This work was supported by NIH R01 EY02416 and the McKnight Scholarship Award to W. W., the NSF GRFP DGE-1746045 to J.D., NIH F31 EY029156 to H.E.A., the NSF Career Award 1652617 and the Physics of Biological Function PHY-1734030 to S.E.P., and NIH RO1 EY012793 to D.B.

Competing Interests

All authors would like to report no competing interests.

562 **Methods**
563
564 **Animals**
565 *Chat-IRES-Cre* mice (129S6-Chat$^{tm2(cre)Lowl}$/J) and floxed *tdTomato* mice (129S6-
566 *Gt(ROSA)26Sor$^{tm9(CAG-tdTomato)Hze}$*/J) were acquired from the Jackson Laboratory. *Drd4-*
567 *GFP* mice were originally developed by MMRRC
568 (http://www.mmrrc.org/strains/231/0231.html) and were backcrossed to the C57BL/6
569 background. These lines were crossed so that both pDSGCs and SACs were labeled.
570 *Vglut2-IRES-Cre* mice and floxed *Ai95(RCL-GCaMP6f)-D* mice were acquired from
571 Jackson Laboratory and were crossed and used for calcium imaging experiments. Mice
572 of ages P21 – P60 of either sex were used. All procedures regarding the use of mice
573 were in accordance with the University of Chicago Institutional Animal Care and Use
574 Committee and with the NIH Guide for the Care and Use of Laboratory Animals and the
575 Public Health Service Policy.
576
577 **Whole-mount retina preparation**
578 Mice were dark adapted for 1 hour and then were anesthetized with isoflurane and
579 euthanized by decapitation. Retinas were isolated at room temperature in oxygenated
580 Ames' medium (Sigma-Aldrich, St. Louis, MO) under infrared illumination. The retinas
581 were separated into dorsal and ventral halves and were mounted ganglion-cell-layer up
582 on top of a ~1.5 mm^2 hole in a small piece of filter paper (Millipore, Billerica, MA). The
583 orientation of the posterior, anterior, inferior, and superior directions were noted for each
584 piece. During the experimental day, the mounted retinas were kept in darkness at room
585 temperature in Ames' medium bubbled with 95% O_2/ 5% CO_2 until use (0 – 8h).
586
587 **Visual stimulation**
588 A white organic light-emitting display (OLEDXL, eMagin, Bellevue, WA; 800 X 600 pixel
589 resolution, 60 Hz refresh rate) was controlled by an Intel Core Duo computer with a
590 Windows 7 operating system and was presented to the retina at a resolution of 1.1
591 μm/pixel. Visual stimuli were generated using MATLAB and the Psychophysics Toolbox,
592 and were projected through the condenser lens of the two-photon microscope focused
593 on the photoreceptor layer.
594
595 For the peripheral spot experiments, stationary spots of size 110 μm diameter were
596 presented 165 μm away from the soma of the recorded pDGSC for 2 seconds. At this
597 distance, these spots were presented outside of the dendritic span of the majority of
598 recorded pDSGCs. These spots were presented in 8 different locations
599 pseudorandomized around the recorded pDSGC, with 3 repetitions each.
600

601 For moving bar experiments, a bright moving bar with dimensions 110 μm (width) X 880
602 μm (length) and speed 330 μm/s moved in 8 different pseudorandomized directions
603 across the receptive field of the pDSGC, with 3 – 6 repetitions each. The occluded bar
604 stimulus was the same as the moving bar stimulus except for the addition of a central
605 occluder with a diameter size of 220 μm which obscured the movement of the bar. The
606 size of the occluder was large enough to obscure the entire dendritic span for the
607 majority of recorded pDSGCs.
608
609 For the emergent moving bar experiments where the bar emerged from different
610 locations of the receptive field, a bright moving bar with dimensions 110 μm (width) X
611 440 μm (length) and speed 330 μm/s could start moving pseudorandomly from 13
612 different locations across the receptive field (Figure 5). The bar could move in the
613 preferred or null direction of the recorded cell.
614
615 For the receptive field mapping experiments, bright spots with a 20 μm diameter were
616 presented across the receptive field of the recorded pDSGC. They were shown for 3 – 4
617 repetitions with a duration of 400 ms in a random sequence within an 11 X 11 grid,
618 covering a total area of 220 X 220 μm^2. To examine the kinetics of EPSCs, bright spots
619 with either a 20 μm diameter (for DHβE and gabazine experiments) or a 60 μm diameter
620 (for DHβE experiments) were shown across the receptive field in a random sequence
621 within an 11 X 11 grid for 3 – 4 repetitions. Spots were shown with a duration of 400 ms.
622
623 The light intensity for bright peripheral spot experiments, the moving bar and occlusion
624 experiments, and the receptive field mapping experiments was ~1.6 X 10^4 R*/rod/s.
625
626 **Targeting cells for electrophysiology**
627 Cells were visualized with infrared light (>900 nm) and an IR-sensitive video camera
628 (Watec). DSGCs were targeted with the aid of two-photon microscopy in *Drd4-GFP*
629 mice. Cell identity was confirmed physiologically by extracellular recordings of
630 responses to moving bars and/or by filling the cell with 25 μM Alexa 594 (Life
631 Technologies) to show bistratified dendritic morphology. Because the tissue was aligned
632 on the filter paper, we confirmed that the preferred direction of the spiking responses to
633 moving bar aligned well with the anatomical posterior (visual field coordinate) or nasal
634 (retinal coordinate) direction.
635
636 **Quantification of dendritic morphology**
637 The ON layer of each cell was isolated from a z-stacked image in ImageJ. To calculate
638 the radius, a contour of the dendritic span was made by drawing a boundary around the
639 dendritic tips, and the area within the contour and resulting equivalent radius was
640 calculated. For calculating dendritic length, the On layer from the z-stack projection was

641 traced in NeuronStudio. The two-dimensional trace was then exported to MATLAB.
642 Dendritic length was calculated in MATLAB using a custom-written code. We subdivided
643 the cell into eight sectors for analysis. Sectors extended out from the soma and were
644 aligned to the spot stimulus such that each spot was at the center between each
645 sector's radial boundaries. When computing normalized vector sums (Figures 2B – C,
646 S2A – S2B), total dendritic length in each sector was normalized by the total dendritic
647 length of the cell.
648
649 **Connectomic analysis**
650 The previously published SBEM dataset was used (Ding et al., 2016). Three On-Off
651 DSGCs along the putative anterior-posterior motion axis were identified by their
652 bistratified dendritic morphology and costratification with SAC processes. The anterior-
653 posterior axis of the tissue is estimated by the dendritic orientation of several
654 morphologically distinctive RGC types that are known to align the dorsa-ventral axis,
655 such as Jam-B RGCs (Kay et al., 2011) and F-RGCs (Rousso et al., 2016). The
656 preferred directions of On-Off DSGC were estimated by weighting the orientation of
657 SAC dendritic inputs onto the DSGC dendrites, since SAC dendrites oriented in the null
658 direction of the DSGC preferentially form GABAergic synapses with DSGCs. Ribbon
659 synapses from On bipolar cells onto DSGC dendrites were manually annotated. All
660 analyses were performed by tracing skeletons and annotating synapses using the
661 Knossos software package (https://knossostool.org/).
662
663 To measure local ribbon density across the DSGC dendritic field, the dendritic span was
664 divided into individual squares with 10 x 10 μm (Figure S4) or 20 x 20 μm (Figure 4)
665 dimensions. Total dendritic length in each square was calculated in Matlab with a
666 custom-written code. The total number of ribbon synapses in each square was also
667 quantified. Ribbon density was calculated by dividing the ribbon synapse number by the
668 total dendritic length in the appropriate squares.
669
670
671 **Electrophysiology recordings**
672 Recording electrodes of 3 – 5 MΩ were filled with a cesium-based internal solution
673 containing 110 mM CsMeSO4, 2.8 mM NaCl, 4 mM EGTA, 5 mM TEA-Cl, 4 mM
674 adenosine 5′-triphosphate (magnesium salt), 0.3 mM guanosine 5′-triphosphate
675 (trisodium salt), 20 mM HEPES, 10 mM phosphocreatine (disodium salt), 5 mM N-
676 Ethyllidocaine chloride (QX314),filled with a cesium-based internal solution containing
677 110 mM CsMeSO4, 2.8 mM NaCl, 4 mM EGTA, 5 mM TEA-Cl, 4 mM adenosine 5′-
678 triphosphate (magnesium salt), 0.3 mM guanosine 5′-triphosphate (trisodium salt), 20
679 mM HEPES, 10 mM phosphocreatine (disodium salt), 5 mM N-Ethyllidocaine chloride

680 (QX314), and 0.025 mM Alexa 594, pH 7.25. Retinas were kept in oxygenated Ames'
681 medium with a bath temperature of 32 – 34 °C.
682
683 Data were acquired using PCLAMP 10 and a Multiclamp 700B amplifier (Molecular
684 Devices, Sunnyvale, CA), low-pass filtered at 4 kHz and digitized at 10 kHz. Light
685 evoked EPSCs were isolated by holding cells at -60 mV after correction for the liquid
686 junction potential (~10 mV).
687
688 To isolate the contribution of synaptic inputs, a host of pharmacological agents were
689 perfused in the bath during electrophysiology recordings. 8 μM Dihydro-b-erythroidine
690 hydrobromide (DHβE; from Tocris, Cat#2349); 10 μM SR 9551 hydrobromide
691 (gabazine; from Tocris, Cat #1262); 100 μM Meclofenamic acid sodium salt (MFA; from
692 Sigma-Aldrich. Cat#M4531); 1 μM Strychnine (from Sigma-Aldrich, Cat#S0532); 50 μM
693 TPMPA (from Tocris, Cat#1040).
694
695 **Data analysis of electrophysiological recordings**
696 Spiking data from loose-patch recordings were analyzed using custom protocols in
697 MATLAB. The number of spikes evoked by the On response to the peripheral spots
698 were quantified in MATLAB and averaged across 3 repetitions in 8 spatial locations.
699 Light-evoked EPSC responses to peripheral spots were obtained as well, and 3
700 repetitions of EPSC traces were averaged to obtain the mean peak amplitude and
701 charge transfer response to each condition. The RSI is determined by (Max - Opp)/(Max
702 + Opp) where Max is the number of spikes, peak amplitude or charge transfer in the
703 region of maximal activation using the peripheral spot stimulus, and Opp is the
704 response in the region directly opposite to the Max region.
705
706 For the receptive field mapping experiments, the light-evoked EPSCs in response to
707 spots sized 20 μm in diameter were obtained and averaged across 3 – 4 repetitions.
708 The center of mass of the receptive field was determined using the EPSC charge
709 transfer or amplitude at each square in the 11 X 11 grid. The dendritic length was
710 calculated at each point on the RF stimulus grid by summing the dendritic length in a
711 circle 60 μm in diameter centered on the square of interest. For maximum vs. opposite
712 region analysis and the preferred side vs null side analysis (Figures 3E and 3F), we
713 considered the EPSCs in two 5 X 5 subsets of the total grid located opposite of each
714 other. The preferred-null side of each cell was determined by spiking responses to the
715 full-field moving bar, and the maximum-opposite axis was determined by EPSC charge
716 transfer responses to the peripheral spot experiment performed in DHβE and gabazine.
717 The distance from soma at each grid location was defined as the distance between the
718 center of the square and the soma center.
719

720 To estimate the spatiotemporal profile across the maximum-opposite or the preferred-
721 null axis for cells in DHβE and gabazine, the light-evoked EPSCs in response to small
722 spots sized 20 μm in diameter were obtained and averaged across 3 – 4 repetitions
723 (Figures 4F – 4H). To estimate the spatiotemporal profile across the preferred-null axis
724 for cells in DHβE only, the light-evoked EPSCs in response to small spots sized 60 μm
725 in diameter were obtained and averaged across 3 repetitions (Figures S4C –D). For
726 both experiments, EPSC parameters of latency, rise time (10 - 90%), and decay time
727 (90 - 30%) were quantified. The preferred-null axis of each cell was determined by
728 spiking responses to the full-field moving bar, and the maximum-opposite axis was
729 determined by EPSC charge transfer responses to the peripheral spot experiment
730 performed in DHβE and gabazine. The parameters of latency, rise time, and decay time
731 were averaged across the squares at equal distances along the cell's preferred-null axis
732 or maximum-opposite axis.
733
734 Spiking data evoked by the On and Off responses to the moving bar and occlusion
735 stimuli were quantified in MATLAB using 3 – 6 repetitions in 8 different directions.
736 Spiking data evoked by the bar starting in different positions were quantified in MATLAB
737 across 3 repetitions in the preferred and null directions.
738
739 **Calcium imaging in posterior- and anterior-preferring On-Off DSGCs**
740 Genetically encoded calcium indicator GCaMP6f was expressed in all RGCs by
741 crossing *Vglut2-IRES-Cre* mice (JAX 016963-*Slc17a6*$^{tm2(cre)Lowl}$) and floxed *Ai95(RCL-*
742 *GCaMP6f)-D* mice (JAX 028865-*Gt(ROSA)26Sor*$^{tm95.1(CAG-GCaMP6f)Hze}$/J). GCaMP6f
743 fluorescence from isolated retinas was imaged in a customized two-photon laser
744 scanning fluorescence microscope (Bruker Nano Surfaces Division). GCaMP6 was
745 excited by a Ti:sapphire laser (Coherent, Chameleon Ultra II, Santa Clara, CA) tuned to
746 920 nm, and the laser power was adjusted to avoid saturation of the fluorescent signal.
747 Onset of laser scanning induces a transient response in RGCs that adapts to the
748 baseline in ~3 s. Therefore, to ensure the complete adaptation of this laser-induced
749 response and a stable baseline, visual stimuli were given after 10 s of continuous laser
750 scanning. To separate the visual stimulus from GCaMP6 fluorescence, a band-pass
751 filter (Semrock, Rochester, MA) was placed on the OLED to pass blue light peaked at
752 470 nm, while two notched filters (Bruker Nano Surfaces Division) were placed before
753 the photomultiplier tubes to block light of the same wavelength. The objective was a
754 water immersion objective (60x, Olympus LUMPlanFl/IR). Time series of fluorescence
755 were collected at 15–30 Hz.

756 We performed an initial direction selectivity test to identify posterior- and anterior-
757 preferring On-Off DSGCs. We recorded GCaMP6f fluorescence from RGC somas within
758 a 75-μm X 75-μm field of view while presenting a full-field moving bar visual stimulus (a
759 bright moving bar 110 μm (width) X 880 μm (length) moving at 330 μm/s across a 660

760 μm circular mask diameter along 8 different directions). At the onset of each moving bar
761 sweep, a TTL pulse was triggered by the visual stimulus computer and recorded by the
762 imaging software to correlate GCaMP6f signals with the direction of each moving bar.
763 Immediately following acquisition of each time series stack, custom-written MATLAB
764 scripts were used to extract fluorescence over time data from time-series images and
765 sort calcium transient by direction of the moving bar. For each RGC soma, raw
766 GCaMP6f fluorescence traces and tuning curves were plotted. On-Off DSGCs were
767 identified by their characteristic singular-lobe directional tuning curves, DSI values ≥ 0.3,
768 and two fluorescence peaks time-locked to the leading (On) and trailing edge (Off) of
769 the moving bar. On-Off DSGCs with preferred directions along the posterior-anterior
770 axis were then selected for further imaging.

771 Once an On-Off DSGC of interest was identified, the visual stimulus was centered to the
772 soma of that cell and a new field of view was drawn to enclose this cell and some
773 background with no GCaMP6f fluorescence. Full-field and occlusion moving bar visual
774 stimulus were presented to the cells as described above (8 directions, 3-4 repetitions).
775 Time series data was collected and subjected to offline analysis.

776 **Imaging analysis for calcium imaging**
777 Analysis was performed using ImageJ and MATLAB. Regions of interest (ROIs)
778 corresponding to DSGC soma and background were manually selected in ImageJ. The
779 fluorescent time course of each ROI was determined by averaging all pixels within the
780 ROI for each frame. The fluorescence of the background region was subtracted from
781 the raw fluorescent signal of the soma ROIs at each time frame. The visual stimulus
782 included a 3 – 4 second intersweep interval between the end of one sweep and the start
783 of another. Fluorescence intensities during these intersweep intervals were used to
784 create a baseline (F0) trace for each ROI by fitting either a single- or two-term
785 exponential decay function. Fluorescence measurements were then converted to ΔF/F0
786 values by calculating $\Delta F=(F-F0)/F0$ for every datapoint. The transformed traces were
787 then smoothed using an average sliding window of 4 datapoints. ΔF/F0 traces were
788 clipped, sorted by visual stimulus direction (0, 45, 90, 135, 180, 225, 270, and 315
789 degrees), and averaged over 3-4 trials. Prior to further analysis, ROIs were subjected
790 to a response quality test QI = Var[Avg. Resp]/Avg(Var[R(t)]) ≥ 0.45 to ensure
791 consistency across trials. Responses to the full-field and occlusion moving bars were
792 broken up into On and Off components according to the circular mask entrance and exit
793 times of the leading and trailing edge, respectively. Peak, area ΔF/F0, and time of peak
794 values were calculated for On, Off, and the full trace along all 8 directions. Direction
795 selectivity index (DSI), vector sum, and preferred direction were calculated for both On
796 and Off components.
797
798

Statistical analysis

Grouped data are presented as mean ± SEM. The Kolmogorov-Smirnov test was used to test data for normality. Student's t-test was used for statistical comparisons of paired samples in Figures 1 and 2. One-way analysis of variance was performed on grouped data in Figures 5 and 6 and subjected to Bonferroni correction.

For the EPSC/dendritic length vs distance from soma experiments, we performed linear regression analysis using an additional categorical predictor variable indicating the maximum-opposite or the preferred-null side. The p-value associated with interaction term (distance*region) in the resulting model was used to determine whether the slopes are significantly different between the two regions. For the EPSC vs dendritic length experiments, we again performed linear regression with an additional categorical predictor variable indicating the maximum-opposite or preferred-null region. The p-value associated with the categorical predictor in the resulting model was used to determine whether the y-intercepts were significantly different between the two regions. The p-value associated with the categorical predictor was used to determine whether the y-intercepts were significantly different between regions. The number of branches in each square of the grid was determined by a custom MATLAB code.

For the kinetic analyses of EPSC parameters of latency, rise time, and decay time, we performed linear regression analysis to determine whether a statistically significant linear relationship exists between the distance from the soma and each EPSC parameter.

For all data sets, $p < 0.05$ was considered significant. *$p < 0.05$; **$p < 0.01$; ***$p < 0.001$.

Experimental parameters for population model

Experimental data for the spiking response to full-field (73 cells) and occlusion (69 cells) stimuli were obtained. 3 – 6 repetitions were obtained for each full-field or occlusion protocol. The baseline firing rate for each repetition was obtained by binning the spiking response in 25-ms time bins and taking the maximum firing rate during a silent period where no stimulus was displayed, and the baseline firing rate was averaged across all repetitions.

To model the spiking response of the pDSGCs, we binned the spikes evoked by the On response to the motion stimulus in 25-ms time bins and plotted the PSTHs for all 8 motion directions. Then, we fit a rectified sine wave to the PSTH of each pDSGC. We defined the threshold for above-baseline firing to be 4 SD above the baseline firing rate. The onset of the spiking response was determined by the time bin at which the firing rate exceeded the threshold and was immediately followed by a second above-

threshold bin (Rate change method; Levakova et al., 2015). We inspected the spiking response onset times returned by our detection algorithm and manually adjusted the spiking response onset times for 3 out of 91 pDSGCs to match the experimental data.

Onset times of spiking responses to the full-field bar moving in the preferred direction ± 45 degrees were similar to those of the preferred-direction response (Figure S7A, left). Likewise, onset times of spiking responses to the occlusion stimulus moving in the null direction ± 45 degrees were similar to those of the null-direction response (Figure S7A, right). Therefore, we included onset times of spiking responses to motions in the directions ± 45 degrees from the preferred-null motion axis in our analysis. Four-parameter beta distributions were fit to histograms of spiking response onset times for preferred- and null-direction motions (Figure 7C). The four parameters included two shape parameters and two parameters that specify the minimum and maximum of the distribution's range.

To determine the offset of the spiking response, we used the algorithm for identifying spiking response onset. Unlike the protocol for determining spiking response onset, however, the detection algorithm started from the most recent time bin and traversed backwards in time. The offset of the spiking response was defined to be the time bin at which the firing rate exceeded the threshold in two out of three consecutive time bins. For each pDSGC, we calculated the spiking response duration by finding the difference between the spiking response onset and offset times. Furthermore, we calculated the linear correlation between spiking response duration and onset (Figure 7D). Figure S7B shows that using only spiking responses to motion along the preferred-null motion axis and using spiking responses to motion along the preferred-null motion axis as well as motion in the directions 45 degrees away from the preferred-null motion axis yielded consistent results. We also calculated the linear correlation between peak firing rate and spiking response onset, but the correlation was not significant for the full-field protocol (Figure S7C).

Motion direction tuning curves

We computed motion direction tuning curves for all pDSGCs exposed to the full-field moving bar stimulus (73 cells) using the CircStat toolbox in MATLAB developed by P. Berens (2009). The height of each tuning curve was given by the total spike count evoked during the presentation of the full-field moving bar stimulus. We fit a Gaussian function to the histogram of the tuning curve widths (Figure S7E). Figure S7F shows all the normalized motion direction tuning curves. The heights of the tuning curves were rescaled by dividing by their peaks and the widths of the tuning curves were rescaled by dividing by their angular deviation, which is the square-root of twice the circular

878 variance. The normalized tuning curves were fit to a one-term Gaussian model (Figure
879 S7F).
880
881 **One-dimensional population model**
882 In our computational model, we arranged two populations (left motion-preferring and
883 right motion-preferring) of DSGCs in a horizontal one-dimensional array. Each
884 population had 100 cells, and the nearest neighbor distance distribution within each
885 population was Gaussian, with a mean of 39 μm and a SD of 16 μm (Huberman et al.,
886 2009). The spatial positions of the DSGCs between the two populations were
887 uncorrelated.
888
889 Each DSGC's mean spiking response to the moving edge was modeled as a rectified
890 sine wave. The amplitude of the sine wave was given by the peak firing rate, while the
891 period and phase were determined by the spiking response duration and onset time,
892 respectively. For each spatial arrangement of DSGCs, we sampled peak firing rates
893 directly from our experimental data. We sampled spiking response onset times from our
894 four-parameter beta distributions (Figure 7C) and determined the spiking response
895 durations by finding the linear correlation between the two (Figure 7D).
896
897 Noise was introduced into the preferred directions of the DSGCs so that they were not
898 all perfectly aligned with the left/right motion axis. To determine the degree of jitter in a
899 DSGC's preferred direction, we sampled from a uniform distribution ranging from -14.1
900 degrees to +14.1 degrees, where 0 degrees represented a preference for motion
901 directly along the left/right motion axis (Fiscella et al., 2015).
902
903 To determine the motion direction tuning width of each simulated DSGC, we sampled
904 circular variances from a Gaussian distribution fit to the histogram of circular variance of
905 the tuning curves from our experimental data (Figure S7E). We scaled the collapsed
906 tuning curve (Figure S7E) by the sampled tuning width and peak firing rate to obtain the
907 tuning curve. We used the motion direction tuning curve to adjust the peak firing rate of
908 the spiking response according to the jitter in the preferred direction alignment.
909
910 We simulated the DSGC population response to a moving edge traveling from left to
911 right at a constant speed of 330 μm/second. To simulate the occlusion protocol, we
912 introduced an occlusion placed over a left motion-preferring DSGC whose position in
913 space was fixed (approximately the 50th left motion-preferring DSGC). For each spatial
914 arrangement of DSGCs, the simulation was repeated 100 times. The spiking response
915 of each DSGC was discretized in time. At each 25-ms time bin, the firing rate given by
916 the rectified sine wave fit was converted to a mean spike count. The number of spikes
917 generated by a DSGC was obtained by sampling from a Gaussian distribution with this

mean and a sub-Poisson, constant variance of 0.4. The sub-Poisson noise was determined from our experimental data by analyzing the variance of the spiking responses to 6 repetitions of the full-field moving bar (10 cells) and the occlusion stimulus (9 cells) (Figure S7D). The spatial positions of the DSGCs were shuffled in each simulation block for a total of 1000 blocks with 100 repetitions in each block.

A population vector (Dayan and Abbott, 2001) was used to decode the spatial position of the moving bar's leading edge. The position estimate $\hat{x}$ at a given time was the firing rate-weighted average of DSGCs' spatial positions

$$\hat{x} = \frac{\sum_i r_i \tilde{x}_i}{\sum_i r_i}$$

where r_i is the firing rate of the *i*th cell and $\tilde{x}_i \sim \mathcal{N}(x_i, w_i{}^2)$ where x_i is the soma position and w_i the RF width of the *i*th cell. The RF width was taken to be the 1 SD boundary of the Gaussian center profile (Chichilnisky and Kalmar, 2002). RF widths were obtained by scaling the dendritic field radii by 1.25. Dendritic field radii were obtained by sampling from Gaussian distribution with $\mu = 88$ µm and $\sigma = 14.8$ µm. In the population vector decoder, we added 130 µm to the soma position of the occluded DSGC to compensate for the lag of the null-direction response to the occlusion stimulus. Errors are reported as the root mean-square-error in the position estimate (Figure 7E).

References

Barlow, H. B. & Hill, R. M. (1963). Selective sensitivity to direction of movement in ganglion cells of rabbit retina. *Science* **139**, 412–414.

Barlow, H.B., and Levick, W.R. (1965). The mechanism of directionally selective units in rabbit's retina. *J. Physiol*. **178**, 477–504.

Briggman, K.L., Helmstaedter, M., and Denk, W. (2011). Wiring specificity in the direction-selectivity circuit of the retina. *Nature* **471**, 183–188.

Chen, Q., Pei, Z., Koren, D., and Wei, W. (2016). Stimulus-dependent recruitment of lateral inhibition underlies retinal direction selectivity. *Elife* **5**, e21053.

Chiao, C.C., and Masland, R.H. (2003). Contextual tuning of direction-selective retinal ganglion cells. *Nat. Neurosci*. **6**, 1251–1252.

Chichilnisky, E.J. and Kalmar, R.S. (2002). Functional asymmetries in ON and OFF ganglion cells of primate retina. *J. Neurosci.* **22**, 2737–2747.

Cruz-Martín, A., El-Danaf, R.N., Osakada, F., Sriram, B., Dhande, O.S., Nguyen, P.L., Callaway, E.M., Ghosh, A., and Huberman, A.D. (2014). A dedicated circuit links direction-selective retinal ganglion cells to the primary visual cortex. *Nature* **507**, 358–361.

Dayan, P. and Abbott, L. (2001). Theoretical neuroscience - computational and mathematical modeling of neural systems. Cambridge, MA: MIT Press.

Demb, J. B., Haarsma, L., Freed, M. A. and Sterling, P. (1999). Functional circuitry of the retinal ganglion cell's nonlinear receptive field. *J. Neurosci.* **19**, 9756–9767.

Deny, S., Ferrari, U., Macé, E., Yger, P., Caplette, R., Picaud, S., Tkačik, G., and Marre, O. (2017). Multiplexed computations in retinal ganglion cells of a single type. *Nat. Commun.* **8**, 1964.

Dhande, O.S., Stafford, B.K., Lim, J.-H.A., and Huberman, A.D. (2015). Contributions of retinal ganglion cells to subcortical visual processing and behaviors. *Annu. Rev. Vis. Sci.* **1**, 291–328.

Ding, H., Smith, R.G., Poleg-Polsky, A., Diamond, J.S., and Briggman, K.L. (2016). Species-specific wiring for direction selectivity in the mammalian retina. *Nature* **535**, 105–110.

Ellis, E.M., Gauvain, G., Sivyer, B., and Murphy, G.J. (2016). Shared and distinct retinal input to the mouse superior colliculus and dorsal lateral geniculate nucleus. *J. Neurophysiol.* **116***,* 602–610.

Euler, T., Detwiler, P. B. and Denk, W. (2002). Directionally selective calcium signals in dendrites of starburst amacrine cells. *Nature* **418**, 845–852.

Famiglietti, E. V. (1983). "Starburst" amacrine cells and cholinergic neurons: mirror-symmetric ON and OFF amacrine cells of rabbit retina. *Brain Res.* **261**, 138–144.

Fiscella, M., Franke, F., Farrow, K., Müller, J., Roska, B., da Silveira, R.A., and Hierlemann, A. (2015). Visual coding with a population of direction-selective neurons. *J. Neurophysiol.* **114**, 2485–2499.

997 Franke, K., Berens, P., Schubert, T., Bethge, M., Euler, T., and Baden, T. (2017).
998 Inhibition decorrelates visual feature representations in the inner retina. *Nature* **542**,
999 439–444.
1000
1001 Fried, S.I., Münch, T.A., and Werblin, F.S. (2002). Mechanisms and circuitry underlying
1002 directional selectivity in the retina. *Nature* **420**, 411–414.
1003
1004 Grzywacz, N.M., and Amthor, F.R. (2007). Robust directional computation in on-off
1005 directionally selective ganglion cells of rabbit retina. *Vis. Neurosci.* **24**, 647–661.
1006
1007 He, S., Jin, Z.F., and Masland, R.H. (1999). The nondiscriminating zone of directionally
1008 selective retinal ganglion cells: comparison with dendritic structure and implications for
1009 mechanism. *J. Neurosci.* **19**, 8049–8056.
1010
1011 He, S., and Masland, R.H. (1998). ON direction-selective ganglion cells in the rabbit
1012 retina: Dendritic morphology and pattern of fasciculation. *Vis. Neurosci.* **15**, 369–375.
1013
1014 Huang, X., Rangel, M., Briggman, K.L., and Wei, W. (2019). Neural mechanisms of
1015 contextual modulation in the retinal direction selective circuit. *Nat. Commun.* **10**, 2431.
1016
1017 Huberman, A.D., Wei, W., Elstrott, J., Stafford, B.K., Feller, M.B., and Barres, B.A.
1018 (2009). Genetic identification of an On-Off direction- selective retinal ganglion cell
1019 subtype reveals a layer-specific subcortical map of posterior motion. *Neuron* **62**, 327–
1020 334.
1021
1022 Ishikane, H., Gangi, M., Honda, S., Tachibana, M. (2005). Synchronized retinal
1023 oscillations encode essential information for escape behavior in frogs. *Nat.*
1024 *Neurosci.* **8**, 1087–1095.
1025
1026 Ito, S., and Feldheim, D.A. (2018). The mouse superior colliculus: An emerging model
1027 for studying circuit formation and function. *Front. Neural Circuits* **12**, 10.
1028
1029 Jacoby, J. and Schwartz, G.W. (2017). Three small-receptive-field ganglion cells in the
1030 mouse retina are distinctly tuned to size, speed, and object motion. *J Neurosci.* **37**, 610–625.
1031
1032 Kay, J.N., de la Huerta, I., Kim, I.J., Zhang, Y., Yamagata, M., Chu, M.W., Meister, M.,
1033 and Sanes, J.R. (2011). Retinal ganglion cells with distinct directional preferences differ
1034 in molecular identity, structure, and central projections. *J. Neurosci.* **31**, 7753–7762.
1035

1036 Kim, T., Soto, F., and Kerschensteiner, D. (2015). An excitatory amacrine cell detects
1037 object motion and provides feature-selective input to ganglion cells in the mouse retina.
1038 *Elife* **4**, e08025.
1039
1040 Kittila, C.A., and Massey, S.C. (1997). Pharmacology of directionally selective ganglion
1041 cells in the rabbit retina. *J. Neurophysiol.* **77**, 675–689.
1042
1043 Kühn, N.K., and Gollisch, T. (2019). Activity correlations between direction-selective
1044 retinal ganglion cells synergistically enhance motion decoding from complex visual
1045 scenes. *Neuron* **101**, 963–976.
1046
1047 Lee, S., Kim, K., and Zhou, Z.J. (2010). Role of ACh-GABA cotransmission in detecting
1048 image motion and motion direction. *Neuron* **51**, 787–799.
1049
1050 Lee, S., Zhang, Y., Chen, M., and Zhou, Z.J. (2016). Segregated glycine-glutamate co-
1051 transmission from vGluT3 amacrine cells to contrast-suppressed and contrast-
1052 enhanced retinal circuits. *Neuron* **90**, 27–34.
1053
1054 Levakova, M., Tamborrino, M., Ditlevsen, S., and Lansky, P. (2015). A review of the
1055 methods for neuronal response latency estimation. *Biosystems* **136**, 23–34.
1056
1057 Lipin, M.Y., Rowl Taylor, W., and Smith, R.G. (2015). Inhibitory input to the direction-
1058 selective ganglion cell is saturated at low contrast. *J. Neurophysiol.* **114**, 927–941.
1059
1060 Marre, O., Botella-Soler, V., Simmons, K.D., Mora, T., Tkačik, G., and Berry, M.J.
1061 (2015). High accuracy decoding of dynamical motion from a large retinal population.
1062 *PLoS Comput. Biol.* **11**, e1004304.
1063
1064 Matsumoto, A., Briggman, K.L., and Yonehara, K. (2019). Spatiotemporally asymmetric
1065 excitation supports mammalian retinal motion sensitivity. *Curr. Biol.* **29**, 3277–3288.
1066
1067 Ölveczky, B. P., Baccus, S. A. and Meister, M. (2003). Segregation of object and
1068 background motion in the retina. *Nature* **423**, 401–408.
1069
1070 Oyster, C.W., and Barlow, H.B. (1967). Direction-selective units in rabbit retina:
1071 Distribution of preferred directions. *Science* **155**, 841–842.
1072
1073 Rivlin-Etzion M., Zhou K., Wei W., Elstrott J., Nguyen P.L., Barres B.A., Huberman A.D.,
1074 and Feller M.B. (2011). Transgenic mice reveal unexpected diversity of On-Off

1075 direction-selective retinal ganglion cell subtypes and brain structures involved in motion
1076 processing. *J Neurosci.* **31**, 8760–8769.
1077
1078 Rousso, D.L.L., Qiao, M., Kagan, R.D.D., Yamagata, M., Palmiter, R.D.D., and Sanes,
1079 J.R.R. (2016). Two pairs of ON and OFF retinal ganglion cells are defined by
1080 intersectional patterns of transcription factor expression. *Cell Rep*. **15**, 1930–1944.
1081
1082 Sabbah, S., Gemmer, J.A., Bhatia-Lin, A., Manoff, G., Castro, G., Siegel, J.K., Jeffery,
1083 N., and Berson, D.M. (2017). A retinal code for motion along the gravitational and body
1084 axes. *Nature* **546**, 492–497.
1085
1086 Sanes, J.R. and Masland R.H. (2015). The types of retinal ganglion cells: current
1087 Status and implications for neuronal classification. *Ann. Rev. Neurosci.* **38**, 221–246.
1088
1089 Schwartz, G., Taylor, S., Fisher, C., Harris, R., and Berry, M.J., II (2007). Synchronized
1090 firing among retinal ganglion cells signals motion reversal. *Neuron* **55**, 958–969.
1091
1092 Sethuramanujam, S., McLaughlin, A.J., deRosenroll, G., Hoggarth, A., Schwab, D.J.,
1093 and Awatramani, G.B. (2016). A central role for mixed acetylcholine/GABA transmission
1094 in direction coding in the retina. *Neuron* **90**, 1243–1256.
1095
1096 Sivyer, B., van Wyk, M., Vaney, D.I., and Taylor, W.R. (2010). Synaptic inputs and
1097 timing underlying the velocity tuning of direction-selective ganglion cells in rabbit retina.
1098 *J. Physiol.* **588**, 3243–3253.
1099
1100 Shi, X., Barchini, J., Ledesma, H.A., Koren, D., Jin, Y., Liu, X., Wei, W., and Cang, J.
1101 (2017). Retinal origin of direction selectivity in the superior colliculus. *Nat. Neurosci.* **20**,
1102 550–558.
1103
1104 Spruston, N. (2008). Pyramidal neurons: dendritic structure and synaptic integration.
1105 *Nat. Neurosci. Reviews* **9**, 206–221.
1106
1107 Takeshita, D., and Gollisch, T. (2014). Nonlinear spatial integration in the receptive field
1108 surround of retinal ganglion cells. *J. Neurosci.* **34**, 7548–7561.
1109
1110 Taylor, W.R., and Vaney, D.I. (2002). Diverse synaptic mechanisms generate direction
1111 selectivity in the rabbit retina. *J. Neurosci.* **22**, 7712–7720.
1112
1113 Trenholm, S., Johnson, K., Li, X., Smith, R.G., and Awatramani, G.B. (2011). Parallel
1114 mechanisms encode direction in the retina. *Neuron* **71**, 683–694.

Turner, M.H., Schwartz, G.W., and Rieke, F. (2018). Receptive field center-surround interactions mediate context-dependent spatial contrast encoding in the retina. *Elife* **7**, e38841.

Wei, W., Hamby, A.M., Zhou, K., and Feller, M.B. (2011). Development of asymmetric inhibition underlying direction selectivity in the retina. *Nature* **469**, 402–406.

Wyatt, H.J., and Daw, N.W. (1975). Directionally sensitive ganglion cells in the rabbit retina: specificity for stimulus direction, size and speed. *J. Neurophysiol.* **38**, 613–626.

Yonehara, K., Balint, K., Noda, M., Nagel, G., Bamberg, E., and Roska, B. (2011). Spatially asymmetric reorganization of inhibition establishes a motion-sensitive circuit. *Nature* **469**, 407–410.

Zhang, Y., Kim, I.J., Sanes, J.R., and Meister, M. (2012). The most numerous ganglion cell type of the mouse retina is a selective feature detector. *Proc. Natl. Acad. Sci. U. S. A.* **109**, E2391–E21398.

Zylberberg, J., Cafaro, J., Turner, M.H., Shea-Brown, E., and Rieke, F. (2016). Direction-selective circuits shape noise to ensure a precise population code. *Neuron* **89**, 369–383.